APPLIED MATHEMATICS AND COMPUTATION

https://www.journals.elsevier.com/applied-mathematics-and-computation

Impact Factor: *3.472*

Accepted June 27th 2021

ASYMPTOTIC STUDY OF UNSTEADY MASS TRANSFER THROUGH A RIGID ARTERY WITH MULTIPLE IRREGULAR STENOSES

Ashis Kumar Roy[a]* and O. Anwar Bég[b]

[a]Department of Science & Humanities, Tripura Institute of Technology, Agartala, Tripura-799009, ***India***

[b]Professor and Director, Multi-Physical Engineering Sciences Group, Mechanical Engineering Department, School of Science, Engineering and Environment (SEE), University of Salford, Manchester, ***UK***

****Corresponding Author: Email:*** *rk.ashis10@gmail.com*

Abstract- The present article examines the transport of species in streaming blood through a rigid artery in the presence of multi-irregular stenosis. The carrier fluid i.e., blood is assumed to be non-Newtonian fluid (Casson's viscoplastic model is used) and the arterial wall is considered to be rigid. A robust model is developed for non-Newtonian flow and hydrodynamic dispersion with first-order chemical reaction on the arterial boundary in multiple irregular stenosed arterial geometries. Multiple scale solutions of the non-dimensional boundary value problem are presented. Asymptotic expressions are developed for velocity and shear stress. Extensive visualization of velocity, concentration, and other flow characteristics is included for various stenotic scenarios, Péclet numbers, and Damköhler numbers. Significant modification in hemodynamic characteristics is computed with viscoplasticity. Mean concentration is also dramatically modified with yield stress and Péclet and Damköhler numbers

Keywords- *Multiple scale analysis, Arterial stenosis, Damköhler number, reaction; Casson viscoplastic model; hemo-rheology; axisymmetric flow; Péclet number*

1.INTRODUCTION

The wide occurrence of hematological diseases worldwide provides a strong motivation

to continuously refine mathematical models of blood flow in the human circulatory system. Many ailments are related intimately to the obstruction of blood flow in arteries and examples include congenital or acquired constrictions, renal arterial stenosis, arteriosclerosis (associated with fatty deposits), coarctation of the aorta, etc. [1]. Pulsatile flow is generated by the rhythmic pumping action of the human heart. It is fundamental to all hemodynamic studies and an excellent exposition of many aspects of pulsatile biophysics including branching trees, perfusion, vascular wall effects, and pathophysiology has been presented by Zamir [2]. Many areas of pulsatile hydrodynamics have been investigated in recent years including ophthalmology [3]. Theoretical, computational, and laboratory models of such flows have provided an indispensable insight into the intrinsic mechanisms involved and an excellent complement to clinical investigations. Many excellent studies have been communicated in particular in the past three decades. Fukushima et al. [4] used glass tube models to visualize horseshoe vortex patterns in pulsatile flow through Y- and T-shaped arterial bifurcations. Moore and Ku [5] employed dye injection to study pulsatile flow patterns in the infrarenal aorta, noting substantial time-dependent variations in the hemodynamics under differing physiological scenarios. Daripa and Dash [6] used an optimized finite difference technique to compute the axial pressure gradient and velocity distribution in pulsatile flow through an eccentric catheterized artery. Boyd and Buick [7] investigated pulsatile blood flow in a three-dimensional carotid artery geometry using the lattice Boltzmann method, considering a number of conditions under a physiologically realistic velocity waveform. These studies have however generally been confined to the Newtonian model for blood flow. At low shear rates, even in large arteries, blood exhibits non-Newtonian characteristics. The presence of multiple suspensions (proteins, fats, ions, red and white blood cells, etc) generates markedly rheological properties in blood. To

more precisely simulate shear stress-strain characteristics of actual blood, therefore rheological models are required and these are invariably adopted from polymer physics and chemical engineering for which they were originally developed. Many excellent and robust formulations have been adopted in hemodynamics including the Maxwell upper convected (UCM) viscoelastic models, FENE-P (finitely extensible nonlinear elastic-Peterlin) model, Oldroyd-B models, Williamson fluids, Vocaldo viscoplastic models, Walters-B short memory fluid models, etc. Zaman et al. [8] used a forward time centered space numerical difference algorithm to compute the pulsatile hemodynamic flow in multi-phase blood through a rigid cylindrical vessel using a Sisko power-law model for the core region and a Newtonian model for the peripheral layer. Ponalagusamy [9] deployed the Herschel-Bulkley model to derive perturbation solutions for pulsating flow in tapered blood vessels. At low shear rates, the viscosity of the blood increases as the red blood cells accumulate at the center of the blood vessel. This accumulation results in the blood behaving as a semi-solid and forming a plug region where no velocity shear can be seen. This behavior can be modeled mathematically by incorporating the idea of yield stress. The yield stress for blood depends on other rheological parameters including hematocrit, temperature, fibrinogen concentration, and under normal conditions, the yield stress of human blood ranges from 0.01 to 0.06 dyn/cm2 as noted by Chandran et al. [10]. A particularly popular model in simulating plug flow is the Casson model [11] which was originally formulated to simulate printing inks in the 1950s. Blair [12] and later Copley [13] have shown that the Casson viscoplastic fluid model provides a robust model for the simple shear behavior of blood in narrow arteries, confirming that at low shear rates the yield stress for blood is non-zero. Merrill et al. [14] demonstrated that blood flow in tubes with a diameter of 130–1000 μm can be reasonably accurately modeled with the Casson model. Charm and Kurland [15] later indicated that the Casson model can also simulate

human blood at a wide range of hematocrit and shear rates. Extensive elaboration of applications of the Casson model in hemodynamics has also been documented by Blair and Spanner [16] . A seminal study of pulsatile hemodynamics using the Casson model was presented by Aroesty and Gross [17] who considered arterioles, venules, and capillaries simulating the core flow with Casson theory and the lower viscosity wall layer as Newtonian. They observed that the plasma layer achieves enhanced lubrication when the effective shear viscosity is much greater than the ultimate high shear viscosity and that this can be beneficial in hemorrhagic shock. Chaturani and Palanisamu [18] used a finite difference technique to compute the pulsatile Casson blood flow under periodic body acceleration and considered the three cases of the wide (femoral) and narrow (arteriole and coronary) tubes. They noted that initial transient time exhibits trivial modifications with yield stress in narrow tubes whereas it is strongly reduced in wide vessels with yield stress. They also observed that axial velocity, wall shear amplitude, and fluid acceleration variations with yield stress are non-uniform only in wider vessels. The Casson model has also been successfully utilized in symplectic cilia-driven propulsion of magnetized blood flow by Akbar et al. [19] (for biomagnetic flow devices) and in periodic blood flow in small vessels by Rohlf and Tenti [20] (who conducted a perturbation analysis using Womersley number i.e. product of Reynolds and Strouhal number as the perturbation parameter).

The above studies were confined to purely fluid flow and ignored mass diffusion or dispersion effects. A primary role of the cardiovascular system is to transport nutrients and oxygen to cells and metabolic waste products away from cells. Therefore, transport of species in arterial blood flow is therefore an important area of hemodynamics research. One of the key transport coefficients in hydrodynamic dispersion i.e. the effective dispersion coefficient for shear flow in a Newtonian fluid was first derived analytically

by Taylor [21] in which experimental verification was also included. This original foundational work was motivated by an aim to theoretically characterize the transport of soluble salt in blood flows and to develop a means for accurately quantifying its molecular diffusivity. This approach essentially describes the transverse mean concentration governed by a diffusion equation in a constantly moving coordinate system. It is based on considering the rate of axial dispersion in fully developed steady Newtonian flow in a straight pipe under the conditions that the dispersion be relatively steady and that longitudinal transport is dominated by convection rather than diffusion. Taylor [21] effectively demonstrated that the resulting effective axial diffusivity is proportional to the square of the Peclet number and inversely proportional to the molecular diffusivity. Thereafter the mathematical fluid dynamic study of solute dispersion in a shear flow, now popularly known as Taylor dispersion, emerged as a major area of interest. Aris [22] significantly generalized the Taylor model by incorporating axial dispersion. Taylor dispersion in arterial blood flows plays a central rule in mixing and is also fundamental to pharmacodynamics i.e. drug transport the physiological system [23]. Important works on Taylor dispersion in blood flow (based on the Newtonian fluid model) include Barton [24], Mazumder and Das [25], and Paul and Mazumder [26]. Recently Wu et al. [27] have computed in detail the diffusion patterns in Taylor dispersion showing that with a modified approach to the longitudinal normality of the transverse mean concentration at the time scale of R_2 / D (R is the tube radius and D is the molecular diffusivity), the solute concentration is found to be uniformly distributed across a family of invariant curved transverse surfaces rather than the conventional flat cross-sections computed in traditional studies. These investigations have been confined to Newtonian fluids. Taylor's dispersion model has however been deployed in a number of computational non-Newtonian pulsatile blood flow and other physiological studies in recent years. Bhargava

et al. [28] used a variational finite element method and a Carreau shear-thinning rheological model to simulate the magnetized pulsating blood flow in a channel with Taylor dispersion and porous medium drag effects magneto-biofluid flow and mass transfer in a non-Darcian porous medium channel, based on the “pistons at infinity approach”. Zueco and Bég [29] applied an electrothermal finite difference solver (PSPICE) to simulate the pulsatile flow of blood in a rigid channel with a dual non-Newtonian formulation (Stokes polar model and the Eyring-Powell model), also considering wall lateral mass flux. Bég et al. [30] used both implicit finite difference and finite element methods to examine the hydromagnetic blood flow and drug dispersion in a permeable channel with the Nakamura-Swada bi-viscosity model. Kiran et al.[31] obtained asymptotic solutions for peristaltic digestive pumping flow and reactive hydrodynamic dispersion in a distensible conduit using the Eringen micropolar fluid model. Several researchers have also implemented the Casson viscoplastic model in hemodynamic Taylor dispersion analysis. Sharp [32] investigated Taylor dispersion in non-Newtonian fluid flow through circular conduits and channels, considering Casson, Bingham, and Ostwald-DeWaele power-law models. He showed that for a core radius of one-tenth the radius of the tube, the effective axial diffusivity in Casson fluids is reduced to approximately 78% of that in a Newtonian fluid at the same flow. Dash et al. [33] extended the work of Sharp [32] to consider unsteady concentration fields in Casson blood flow using the Gill-Sankarasubramanian generalized dispersion model [34]. Using a generalized dispersion model, Nagarani et al. [35] later studied the solute dispersion in channel and pipe Casson blood flow and discussed the impact of yield stress and irreversible wall reaction on various transport coefficients using asymptotic methods. Rana and Murthy [36] revisited the problem in [35] with the motivation of estimating the time-dependent transport coefficients. Recently, Roy et al. [37] and Debnath et al. [38,

39] highlighted the impact of various factors on the dispersion transport coefficient in Casson blood flows.

The flow-through blood vessels are adversely affected when an obstruction arises. The deviation in blood flow from the natural healthy state, as noted earlier, manifests in many deadly diseases including atherosclerosis. Arterial stenosis is a consequence of atherosclerosis and is essentially a constriction in the blood vessel induced by undesirable deposits on the arterial walls [40]. The blood flow is disrupted by the accumulation of fats, lipids, cholesterol, and fibrous tissues at the inner walls of the blood vessel, leading to heart diseases and conditions including cardiac arrest, cardiac ischemia, brain ischemia, etc. Due to the immense clinical significance of stenotic hemodynamics, it has become a major focus in modern physiological fluid dynamics and has been increasingly studied with the acceleration in computer hardware and improvement in numerical methods. This research thrust aims ultimately to mitigate such ailments via a deeper understanding of the root causes of these diseases and the development of suitable bioengineering methods for their elimination. Although significant work has been done on Newtonian flows in stenosed arterial geometries, non-Newtonian hemo-rheological flows have only quite recently received attention. Zaman et al. [41] used finite difference methods to simulate micropolar blood flow in a tapered arterial segment featuring both stenosis (constriction) and aneurysm (bulge). Zaman et al. [42] deployed a penalty finite element technique to analyze time-dependent viscoelastic blood flow in a W-shaped stenotic artery. Ali et al. [43] further investigated the dispersion of nanoparticles in pharmacological transport in Carreau blood flow through a converging stenotic zone also considering heat transfer effects. Dubey et al [44] used the FREEFEM++ finite element code to compute the core (Casson viscoplastic fluid) and peripheral (Sisko viscoelastic model) pulsatile hemodynamics in a cylindrical conduit doped with nanoparticles and featuring stenosis

followed by an aneurysm. Srivastava and Saxena [45] simulated the blood flow through an artery with mild stenosis in which the core region was modeled as a Casson fluid and the peripheral layer of plasma as a Newtonian fluid. They observed that hemodynamic impedance and wall shear stress (WSS) are both suppressed with a decrease in peripheral layer viscosity. Very recently Priyadharshini and Ponalagusamy [46] have very recently investigated the hydromagnetic pulsatile Casson blood flow conveying nanoparticles in a stenosed artery with a periodic body acceleration using a finite difference scheme. They computed the influence of stenotic height, yield stress, magnetic field, particle concentration, and mass parameters on wall shear stress, flow resistance, and velocity profiles. Increased nanoparticle doping, stronger magnetic field, and higher yield stress were all found to expand notably the plug core radius. These studies have been restricted however to regular stenotic geometries. A number of coronary arterial diseases exhibit irregular stenoses which require more sophisticated geometrical models for their accurate simulation. These may also occur in a multiple fashion over protracted lengths of the artery. Numerical analyses of such systems, therefore, furnishes a more realistic appraisal of clinical situations. Several studies have appeared in the last decade considering multi-irregular stenotic blood flows. Mustapha et al. [47] used the Harlow-Welch marker and cell (MAC) and successive-over-relaxation (SOR) method to study the time-dependent Newtonian blood flow in an arterial segment in the presence of dual stenoses featuring surface irregularities. They observed that the hydrodynamic flow pattern exhibits a separation Reynolds number for the multi-irregular stenoses which is significantly lower than those for cosine-shaped stenoses and a long single irregular stenosis. They also found that cosine stenoses produce a higher pressure drop compared with irregular ones. Other interesting studies of irregular stenotic hemodynamics include Johnston and Kilpatrick [48] and Andersson et al. [49], again both for Newtonian fluids. Chakravarty et al. [50]

used a finite volume, immersed boundary and finite element methods to study Newtonian irregular stenotic hemodynamics, noting that improvements to the simulations were required via incorporation of heterogeneity of the vascular wall and non-Newtonian rheology of the streaming blood. Further analysis of Newtonian blood flow in irregular stenotic regions with body acceleration has been reported by Mustapha et al. [51].

Mass transfer in stenosed arteries has also received some attention owing to applications in nutrient transport. Fowler et al. [52] conducted an early study of the relative contributions of venous admixture and pulmonary oxygen diffusing capacity to the alveolar-arterial oxygen tension gradient in multiple patients with stenosed arteries. More recently valencia and Villaneuva [53] used the ADINA finite element code to simulate unsteady non-Newtonian blood flow and mass transfer with full-body fluid-structure interaction in symmetric and non-symmetric stenotic arteries. They employed a hyperviscosity blood model and hyperelastic Mooney–Rivlin model for the compliant arterial wall and observed that wall distensibility significantly modifies the hemodynamics and furthermore that the stenosis length and depth impact substantially on recirculation length, and distribution of concentration of macromolecules, such as low-density lipoproteins (LDL). Zaman et al. [54] have simulated the combined heat and mass transfer in tapered artery hemodynamics with an overlapping stenosis using the Cross non-Newtonian model. Further studies include Olgac et al. [55], Kaazempur-Mofrad et al. [56], and Yang and Vafai [57].

The above studies however have not simultaneously considered non-Newtonian flow and Taylor hydrodynamic dispersion with the first-order chemical reaction on the arterial boundary in multiple irregular stenosed arterial geometries. This is the novelty of the present work which aims to provide a more comprehensive multi-physico-chemical simulation of obstructed arterial flow. The Casson model is employed for blood rheology.

We develop multiple-scale solutions of the non-dimensional boundary value problem. asymptotic expressions are developed for velocity and shear stress. Extensive visualization of velocity, concentration, and other flow characteristics is included for various stenotic scenarios, Péclet numbers, and Damköhler numbers. The study is relevant to oxygen transport in realistic physiological systems [58] and plaque deposition in the intima layer of arteries (atherogenesis) [59, 60]. To the best of our knowledge, the present work constitutes a novel contribution to stenotic hemodynamic transport modeling.

2. MATHEMATICAL MODEL

2.1 Mass Transfer Model

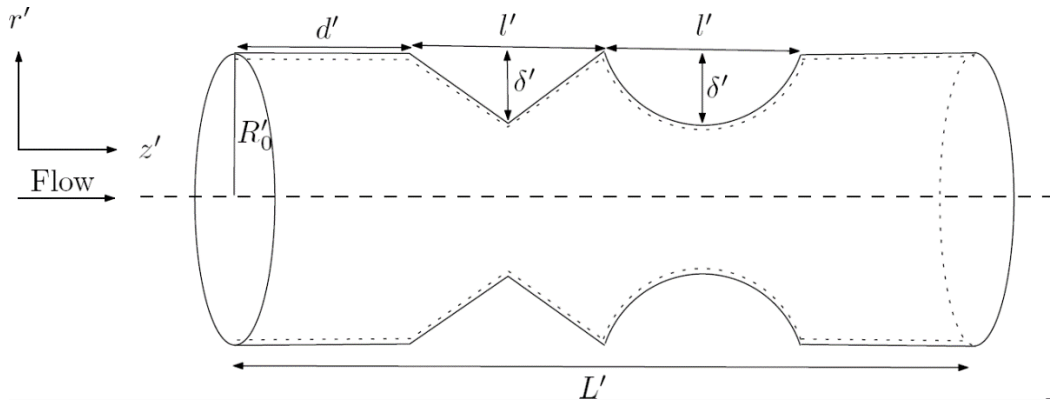

Fig. 1: Schematic diagram of axisymmetric blood flow in an irregular multi-stenosed vessel.

Consider the solute dispersion in fully developed incompressible viscous non-Newtonian blood flow through a rigid artery in the presence of axially symmetrical multi-irregular stenoses. The concentration $C'(z',r',t')$ of the species dissolved in the blood is governed by the following partial differential equation:

$$\frac{\partial C'}{\partial t'}+u'(r',t')\frac{\partial C'}{\partial z'}=D\frac{\partial^2 C'}{\partial z'^2}+\frac{D}{r'}\frac{\partial}{\partial r'}\left(r'\frac{\partial C'}{\partial r'}\right)\ \ \textbf{in}\Omega'\times(0,T'), \tag{1}$$

here D denotes constant molecular diffusivity of the species in blood, $u'(r',z')$ is blood velocity while Ω' represents the geometry of the stenosed artery which is defined with the following expression:

$$\Omega' = \left\{(z', r') \in ¡^{2} : 0 < z' < L', 0 < r' < R'(z') = R_0' - \xi'(z')\right\}. \quad (2)$$

Where:

$$\xi'(z') = \begin{cases} \frac{2\delta'}{l'}\left(z' - d'\right), & d' \le z' \le d' + \frac{l'}{2}, \\ -\frac{2\delta'}{l'}\left(z' - d' - l'\right), & d' + \frac{l'}{2} \le z' \le d' + l', \\ \delta' - \frac{4\delta'}{l'^2}\left(z' - d' - \frac{3l'}{3}\right)^2, & d' + l' \le z' \le d' + 2l', \\ 0, & \text{otherwise.} \end{cases}, \quad (3)$$

Where l' and δ' length and critical height of the stenosis, respectively. A cylindrical coordinate system (r', θ', z'). is considered to describe the model (**Fig.** 1), where L' is the length of the artery. We presume that the solute molecules do not react with each other; however, they undergo a *first-order chemical reaction* on the arterial boundary at a constant rate Γ' defined by:

$$-D\frac{\partial C'}{\partial r'} = \Gamma' C' \qquad \text{on} \quad \partial\Omega' \times (0, T'), \quad (4)$$

where $\partial\Omega' = \left\{(z', r') \in ¡^{2} : 0 < z' < L', r' = R'(z')\right\}$. Also, due to symmetry:

$$\frac{\partial C'}{\partial r'} = 0 \qquad \text{at} \quad r' = 0. \quad (5)$$

The initial and upstream and downstream condition is taken as:

$$C'(z', r', 0) = \frac{Q\delta(z')}{\pi R_0'^2}, \quad (6)$$

$$C'(\pm\infty, r', t') = 0. \quad (7)$$

where Q is the mass of the species released in the blood flow and $\delta(\cdot)$ is the direct delta function.

The blood considered in this study is assumed to be non-Newtonian Casson fluid which is known to approximate quite accurately hemodynamic characteristics at low shear rates. The appropriate momentum equation for steady one-dimensional shear flow is:

$$-\frac{\partial p'}{\partial z'}=\frac{1}{r'}\frac{\partial}{\partial r'}(r'\tau') \text{ in } \Omega'. \tag{8}$$

The axial periodic pressure gradient $\partial p'/\partial z'$ is assumed to be constant. τ' is shear stress of the Casson fluid which obeys the following constitutive equation [37].

$$-\frac{\partial u'}{\partial r'}=\begin{cases}\frac{1}{\mu'}\left(\sqrt{\tau'}-\sqrt{\tau'_y}\right)^2 & \text{if} \quad \tau'\geq\tau'_y \\ 0 & \text{if} \quad \tau'\leq\tau'_y\end{cases} \tag{9}$$

The quantities, μ' and τ'_y in Eq. (9), are viscosity and the yield stress of the blood, respectively. The boundary conditions for the regime may be prescribed as:

$$\left.\begin{aligned}&u'(r',z')=0, \quad \text{on} \quad \partial\Omega' \\ &\tau'(r',z')<\infty, \quad \text{at} \quad r'=0.\end{aligned}\right\} \tag{10}$$

The first condition in Eq. (10) describes the classical no-slip boundary condition whereas the second condition depicts the finite shear stress at the center of the arterial geometry. Let us now introduce the following set of normalized variables, where quantities with a prime indicate that they are dimensional:

$$\begin{aligned}&r=\frac{r'}{R'_0},\ (\xi,\delta)=(\xi',\delta')\frac{L'}{R'^2_0},\ (z,l,d)=(z',l',d')/L',\ t=\frac{t'}{T_R},\ u=\frac{u'}{u_R}, \\ &C=\frac{C'}{C_R},\ \Gamma=\frac{\Gamma'}{\Gamma_R},\ \tau=\frac{\tau' R'}{\mu' u_R},\tau_y=\frac{\tau'_y R'_0}{\mu' u_R}\end{aligned} \tag{11}$$

The subscript *R* used above denotes reference variables. By virtue of Eq. (11), the mass transport (species diffusion) problem defined by Eqs. (1 -5) is readily transformed to:

$$\begin{cases}\frac{\partial C}{\partial t}+\frac{u_R T_R}{L}u(r,z)\frac{\partial C}{\partial z}=\frac{DT_R}{L'^2}\frac{\partial^2 C}{\partial z^2}+\frac{DT_R}{R'^2_0}\frac{1}{r}\frac{\partial}{\partial r}\left(r\frac{\partial C}{\partial r}\right) & \text{in} \quad \Omega\times(0,T), \\ -\frac{D}{\Gamma_R R'_0}\frac{\partial C}{\partial r}=\Gamma C & \text{on} \quad \partial\Omega\times(0,T), \\ \frac{\partial C}{\partial r}=0 & \text{at} \quad r=0,\end{cases} \tag{12}$$

with

$$\Omega=\left\{(z,r)\in \mathbb{R}^2 : 0<z<1, 0<r<1-\varepsilon\xi(z)\right\}, \tag{13}$$

$$\partial\Omega=\left\{(z,r)\in \mathbb{R}^2 : 0<z<1, r=1-\varepsilon\xi(z)\right\}, \tag{14}$$

$$\xi(z)=\begin{cases}\dfrac{2\delta}{l}(z-d), & d\le z\le d+\dfrac{l}{2},\\ -\dfrac{2\delta}{l}(z-d-l), & d+\dfrac{l}{2}\le z\le d+l,\\ \delta-\dfrac{4\delta}{l^2}\left(z-d-\dfrac{3l}{3}\right)^2, & d+l\le z\le d+2l,\\ 0, & \text{otherwise.}\end{cases} \tag{15}$$

Choosing the time scale $T_R = L'/u_R$ we arrive at the following dispersion problem:

$$\mathbf{Pe}\varepsilon\left[\frac{\partial C}{\partial t}+u(r,z)\frac{\partial C}{\partial z}\right]=\varepsilon^2\frac{\partial^2 C}{\partial z^2}+\frac{1}{r}\frac{\partial}{\partial r}\left(r\frac{\partial C}{\partial r}\right) \quad \text{in} \quad \Omega\times(0,T), \tag{16}$$

$$\frac{\partial C}{\partial r}=-\mathbf{Da}\Gamma C \quad \text{on} \quad \partial\Omega\times(0,T), \tag{17}$$

$$\frac{\partial C}{\partial r}=0 \quad \text{at} \quad r=0, \tag{18}$$

The derivation of axial velocity $u(r,z)$ is shown in the **Appendix**. $\mathbf{Pe}=u_R R_0'/D$ and $\mathbf{Da}=T_R R_0'/D$ are the Péclet number and Damköhler numbers respectively. The boundary condition (17) at $r=1-\varepsilon\xi(z)$ can be approximated at $r=1$ using a Taylor series expansion as follows:

$$\frac{\partial C}{\partial r}-\varepsilon\xi\frac{\partial^2 C}{\partial r^2}+\frac{\varepsilon^2\xi^2}{2}\frac{\partial^3 C}{\partial r^3}+\mathrm{O}(\varepsilon^3)=-\mathbf{Da}\Gamma\left[C-\varepsilon\xi\frac{\partial C}{\partial r}+\frac{\varepsilon^2\xi^2}{2}\frac{\partial^2 C}{\partial r^2}+\mathrm{O}(\varepsilon^3)\right] \text{ at } r=1\Big\}. \tag{19}$$

In order to prepare the appropriate foundation for a perturbation analysis, it is assumed that:

The length scale of the axial spreading is much greater than that of radius of the tube artery, i.e., the ratio $R_0'/L'=\varepsilon<<1$.

The stenosis of the artery is mild thus $\delta'/R_0'<<1$ is very small.

Péclet number assumed to be of order unity i.e., $\mathbf{Pe}\sim\mathrm{O}\left(u_R R_0'/D\right)\sim\mathrm{O}(1)$.

Two time scales are considered: *convection time* and *diffusion time* along the artery. Therefore, it follows that:

$$T_0\sim\mathrm{O}\left(\frac{L'}{u_R}\right)\sim\mathrm{O}(1), \tag{20}$$

$$T_1\sim\mathrm{O}\left(\frac{L'^2}{D}\right)\sim\mathrm{O}\left(\frac{L'}{R_0'}\frac{L'}{u_R}\frac{u_R R_0'}{D}\right)\sim\mathrm{O}(1/\varepsilon). \tag{21}$$

Eqns. (18) and (19) imply:

$$T_0 : T_1 = 1 : \frac{1}{\varepsilon}. \tag{22}$$

Based on these time-scales, we may introduce the following relation:

$$t_0 = t,\ t_1 = \varepsilon t. \tag{23}$$

Here t_0 and t_2 indicate dimensionless fast and slow time variables.

$$\therefore \frac{\partial}{\partial t} \to \frac{\partial}{\partial t_0} + \varepsilon \frac{\partial}{\partial t_1}. \tag{24}$$

Surface absorption is assumed to be comparable with advection speed and therefore Damköhler number is of the order of unity i.e; $\mathbf{Da} = \mathrm{O}(\varepsilon)$.

2.2 Asymptotic analysis of the transport coefficient

Using the asymptotic expression for solute concentration, *C*, suggested by Fifa and Nicholes [37], in various time scales as:

$$C(t,r,z) = C_{(0)}(t_0,t_1,r,z) + \varepsilon C_{(1)}(t_0,t_1,r,z) + \varepsilon^2 C_{(2)}(t_0,t_1,r,z) + \mathrm{O}(\varepsilon^3), \tag{25}$$

Now substituting the above expansion in Eqn. (16) we have:

$$\begin{aligned} &\varepsilon \mathbf{Pe} \frac{\partial C_{(0)}}{\partial t_0} + \varepsilon^2 \mathbf{Pe}\left[\frac{\partial C_{(0)}}{\partial t_1} + \frac{\partial C_{(1)}}{\partial t_0}\right] + \varepsilon \mathbf{Pe} u_0(r) \frac{\partial C_{(0)}}{\partial z} \varepsilon^2 \mathbf{Pe}\left[u_0(r)\frac{\partial C_{(1)}}{\partial z} + u_1(r)\frac{\partial C_{(0)}}{\partial z}\right] \\ &= \varepsilon^2 \frac{\partial^2 C_{(0)}}{\partial z^2} + \frac{1}{r}\frac{\partial}{\partial r}\left(r\frac{\partial C_{(0)}}{\partial r}\right) + \varepsilon \frac{1}{r}\frac{\partial}{\partial r}\left(r\frac{\partial C_{(1)}}{\partial r}\right) + \varepsilon^2 \frac{1}{r}\frac{\partial}{\partial r}\left(r\frac{\partial C_{(2)}}{\partial r}\right) + \mathrm{O}(\varepsilon^3) \text{ in } \Omega \times (0,T) \end{aligned} \tag{26}$$

Now, by equating the like powers of ε from both side we have:

$$1 : \frac{1}{r}\frac{\partial}{\partial r}\left(r\frac{\partial C_{(0)}}{\partial r}\right) = 0 \tag{27}$$

$$\varepsilon : \mathbf{Pe}\frac{\partial C_{(0)}}{\partial t_0} + \mathbf{Pe} u_0(r)\frac{\partial C_{(0)}}{\partial z} = \frac{1}{r}\frac{\partial}{\partial r}\left(r\frac{\partial C_{(1)}}{\partial r}\right) \tag{28}$$

$$\varepsilon^2 : \mathbf{Pe}\left[\frac{\partial C_{(0)}}{\partial t_1} + \frac{\partial C_{(1)}}{\partial t_0} + u_0(r)\frac{\partial C_{(1)}}{\partial z} + u_1(r)\frac{\partial C_{(0)}}{\partial z}\right] = \frac{\partial^2 C_{(0)}}{\partial z^2} + \frac{1}{r}\frac{\partial}{\partial r}\left(r\frac{\partial C_{(2)}}{\partial r}\right) \tag{29}$$

The boundary conditions of $C_{(0)}$, $C_{(1)}$ and $C_{(2)}$ are determined using Eqns. (18), (19) and assumptions (e), which are displayed in the equations below:

$$1:\begin{cases}\dfrac{\partial C_{(0)}}{\partial r}=0 & \text{at} \quad r=0\\ \dfrac{\partial C_{(0)}}{\partial r}=0 & \text{at} \quad r=1\end{cases} \tag{30}$$

$$\varepsilon:\begin{cases}\dfrac{\partial C_{(1)}}{\partial r}=0 & \text{at} \quad r=0\\ \dfrac{\partial C_{(1)}}{\partial r}-\xi\dfrac{\partial^2 C_{(0)}}{\partial r^2}=-\Gamma C_{(0)} & \text{at} \quad r=1\end{cases} \tag{31}$$

$$\varepsilon^2:\begin{cases}\dfrac{\partial C_{(2)}}{\partial r}=0 & \text{at} \quad r=0\\ \dfrac{\partial C_{(2)}}{\partial r}-\xi\dfrac{\partial^2 C_{(1)}}{\partial r^2}+\dfrac{\xi^2}{2}\dfrac{\partial^3 C_{(0)}}{\partial r^3}=-\Gamma C_{(1)} & \text{at} \quad r=1\end{cases} \tag{32}$$

2.3.1 Leading order

For leading order Eqn. (27) and (30) assume the form:

$$\frac{1}{r}\frac{\partial}{\partial r}\left(r\frac{\partial C_{(0)}}{\partial r}\right)=0 \tag{33a}$$

$$\frac{\partial C_{(0)}}{\partial r}=0 \quad \text{at } r=0 \tag{33b}$$

$$\frac{\partial C_{(0)}}{\partial r}=0 \quad \text{at } r=1 \tag{33c}$$

Eqns. (33a)-(33c) ensure that the leading order concentration $C_{(0)}$ is independent of r i.e.,

$$C_{(0)}=C_{(0)}(t_0,t_1,z) \tag{34}$$

2.3.2 First order

For the first-order perturbation problem, we have, recalling Eqs. (28) and (31):

$$\mathbf{Pe}\frac{\partial C_{(0)}}{\partial t_0}+\mathbf{Pe}u_0\frac{\partial C_{(0)}}{\partial z}=\frac{1}{r}\frac{\partial}{\partial r}\left(r\frac{\partial C_{(1)}}{\partial r}\right) \tag{35a}$$

$$\frac{\partial C_{(1)}}{\partial r}=0 \quad \text{at } r=0 \tag{35b}$$

$$\frac{\partial C_{(1)}}{\partial r}=-\Gamma C_{(0)} \quad \text{at } r=1 \tag{35c}$$

By taking the section average of Eq. (35a) with the aid of Eqs. (35b) and (35c) yields:

$$\mathbf{Pe}\frac{\partial C_{(0)}}{\partial t_0}+\mathbf{Pe}\left[\frac{1}{2}-\frac{8}{7}\sqrt{r_p}+\frac{2}{3}r_p-\frac{1}{42}r_p^4\right]\frac{\partial C_{(0)}}{\partial z}+2\Gamma C_{(0)}=0 \tag{36}$$

In view of Eq. (36), then Eq. (35a) becomes:

$$\frac{1}{r}\frac{\partial}{\partial r}\left(r\frac{\partial C_{(1)}}{\partial r}\right)=\mathbf{Pe}\left[u_0-\frac{1}{2}+\frac{8}{7}\sqrt{r_p}-\frac{2}{3}r_p+\frac{1}{42}r_p^4\right]\frac{\partial C_{(0)}}{\partial z}-2\Gamma C_{(0)} \tag{37}$$

Next, using the boundary conditions (35b) and (35c) the solution of Eq. (37) emerges as:

$$C_{(1)}=\mathbf{Pe}\mathbf{A}(r)\frac{\partial C_{(0)}}{\partial z}-\frac{\Gamma}{2}C_{(0)}r^2+f(t_0,t_1,z). \tag{38}$$

Where:

$$\mathbf{A}(r)=\begin{cases}-\dfrac{115r_p^4}{7056}-\dfrac{r_p^4}{84}\ln\left(\dfrac{r}{r_p}\right)+\left(\dfrac{1}{8}+\dfrac{r_p^4}{168}-\dfrac{8\sqrt{r_p}}{21}+\dfrac{r_p}{3}\right)r^2 & \\ -\dfrac{2r_p}{9}r^3-\dfrac{r^4}{16}+\dfrac{32\sqrt{r_p}}{147}r^{7/2}, & r\geq r_p \\ \left(\dfrac{1}{8}+\dfrac{r_p}{3}-\dfrac{8\sqrt{r_p}}{21}-\dfrac{r_p^2}{12}+\dfrac{r_p^4}{168}\right)r^2, & r\leq r_p\end{cases} \tag{39}$$

Here $f(t_0,t_1,z)$ is an arbitrary function, and to determine this function we assume $2\int_0^1 rC_{(1)}dr=0$, without loss of generality. This gives:

$$f(t_0,t_1,z)=\mathbf{Pe}\left(\frac{13r_p^4}{1764}+\frac{r_p^6}{1320}-\frac{1}{24}+\frac{60\sqrt{r_p}}{539}-\frac{7r_p}{90}-\frac{r_p^4}{84}\ln(r_p)\right)\frac{\partial C_{(0)}}{\partial z}+\frac{\Gamma}{4}C_{(0)} \tag{40}$$

2.3.2 Second order

Now we recall Eqs. (29) and (32) for the second-order perturbation problem:

$$\begin{aligned}\frac{1}{r}\frac{\partial}{\partial r}\left(r\frac{\partial C_{(2)}}{\partial r}\right) &= \mathbf{Pe}\frac{\partial C_{(0)}}{\partial t_1}+\mathbf{Pe}\frac{\Gamma}{4}\left(1-2r^2\right)\frac{\partial C_{(0)}}{\partial t_0}+ \\ &\quad \mathbf{Pe}\left[\frac{\Gamma}{4}\left(1-2r^2\right)u_0+u_1-2\Gamma\left(\mathbf{A}+X\right)\right]\frac{\partial C_{(0)}}{\partial z} \\ &\quad +\mathbf{Pe}^2\left[\left(u_0-F\right)\left(\mathbf{A}+X\right)-\frac{1}{\mathbf{Pe}^2}\right]\frac{\partial^2 C_{(0)}}{\partial z^2},\end{aligned} \tag{41a}$$

$$\frac{\partial C_{(2)}}{\partial r}=0 \qquad \text{at} \qquad r=0, \tag{41b}$$

$$\frac{\partial C_{(2)}}{\partial r} = -\mathbf{Pe}\left[\xi(z)F + \Gamma\left(\frac{r_p^6}{1320} - \frac{r_p^4}{336} + \frac{r_p}{30} - \frac{4\sqrt{r_p}}{77} + \frac{1}{48}\right)\right]\frac{\partial C_{(0)}}{\partial z} - \left[\frac{\Gamma^2}{4} + \xi(z)\Gamma\right]C_{(0)} \qquad \text{at} \qquad r = 1. \tag{41c}$$

Here the following definitions apply:

$$F = \frac{1}{2} - \frac{8}{7}\sqrt{r_p} + \frac{2}{3}r_p - \frac{1}{42}r_p^4, \tag{42}$$

$$X = \frac{13r_p^4}{1764} + \frac{r_p^6}{1320} - \frac{1}{24} + \frac{60\sqrt{r_p}}{539} - \frac{7r_p}{90} - \frac{r_p^4\ln\left(r_p\right)}{84}. \tag{43}$$

Taking the section average of Eq. (41a) using Eqs.(41b) and (41c) we arrive at:

$$\mathbf{Pe}\frac{\partial C_{(0)}}{\partial t_1} + 2\mathbf{Pe}\left[\xi(z)\left(-\frac{1}{2} - \frac{r_p}{3} + \frac{6\sqrt{r_p}}{7} - \frac{r_p^4}{42}\right) + \Gamma\left(\frac{r_p^6}{660} - \frac{r_p^4}{168} - \frac{8\sqrt{r_p}}{77}a + \frac{r_p}{15} + \frac{1}{24}\right)\right]\frac{\partial C_{(0)}}{\partial z} - \left[1 + \frac{\mathbf{Pe}^2}{192}\left(1 - \frac{5888\sqrt{r_p}}{1155} + \frac{558368r_p}{56595} - \frac{6144r_p^{3/2}}{715} + \frac{128r_p^2}{45} - \frac{8r_p^4}{21} + \frac{3840r_p^{9/2}}{3773} - \frac{32r_p^5}{45} + \frac{8r_p^6}{55} - \frac{512r_p^{13/2}}{1155} + \frac{64r_p^7}{165} - \frac{8r_p^8\ln\left(r_p\right)}{147} - \frac{943r_p^8}{22295} + \frac{8r_p^{10}}{1155}\right)\right]\frac{\partial^2 C_{(0)}}{\partial z^2} + 2\left[\frac{\Gamma^2}{4} + \xi(z)\Gamma\right]C_{(0)} = 0. \tag{44}$$

Now multiplying Eqn. (44) by ε and adding to Eqn. (36) yields:

$$\mathbf{Pe}\frac{\partial C_{(0)}}{\partial t} + \mathbf{Pe}K_1\frac{\partial C_{(0)}}{\partial z} - \varepsilon K_2\frac{\partial^2 C_{(0)}}{\partial z^2} + 2K_0 C_{(0)} = 0, \tag{45}$$

where:

$$K_0 = \Gamma + \frac{\varepsilon\Gamma^2}{4} + \varepsilon\xi(z)\Gamma, \tag{46}$$

$$K_1 = \left(\frac{1}{2} - \frac{8}{7}\sqrt{r_p} + \frac{2}{3}r_p - \frac{1}{42}r_p^4\right) + \varepsilon\xi(z)\left(-1 - \frac{2r_p}{3} + \frac{12\sqrt{r_p}}{7} - \frac{r_p^4}{24}\right) + \Gamma\mathbf{Da}\left(\frac{r_p^6}{330} - \frac{r_p^4}{84} - \frac{16\sqrt{r_p}}{77} + \frac{2r_p}{15} + \frac{1}{12}\right), \tag{47}$$

$$K_2 = 1 + \frac{\mathbf{Pe}^2}{192}\left(1 - \frac{5888\sqrt{r_p}}{1155} + \frac{558368 r_p}{56595} - \frac{6144 r_p^{3/2}}{715} + \frac{128 r_p^2}{45} - \frac{8 r_p^4}{21} + \frac{3840 r_p^{9/2}}{3773} - \frac{32 r_p^5}{45} + \frac{8 r_p^6}{55} - \frac{512 r_p^{13/2}}{1155} + \frac{64 r_p^7}{165} - \frac{8 r_p^8 \ln\left(r_p\right)}{147} - \frac{943 r_p^8}{22295} + \frac{8 r_p^{10}}{1155}\right). \quad (48)$$

The above simplified mathematical model for *zeroth-order concentration* is analogous with the earlier Shanksubramanian-Gill dispersion model [34]. Thus the coefficient of the above equation can be characterized by the reaction (K_0), convection (K_1) , and dispersion (K_2) coefficients (regardless of the signs). The transport coefficients K_0 and K_1 are functions of $\xi(z)$; however, the *dispersion coefficient is not dependent* on $\xi(z)$, and a higher-order correction is required to illustrate the effect of arterial stenosis. The dispersion coefficient is found to match exactly with Dash *et al*. [33]. It is worth mentioning that the perturbation parameter ε corresponds to a pair of dimensionless numbers viz., *aspect ratio*, and *Damkohler number;* the former is associated with the geometry of the problem and the latter corresponds to the reaction at the boundary. In view of this, $\varepsilon\Gamma$ has been replaced by $\mathbf{Da}\Gamma$ whereas $\varepsilon\xi(z)$ remains unchanged in the transport Eqns. (47) and (48). In the absence of arterial stenosis (i.e. $\xi(z) = 0$) and if the blood is assumed to be Newtonian ($r_p = 0$) then the transport coefficients are found to be, respectively:

$$\lim_{\xi(z)\to 0,} K_0 = \Gamma + \frac{\mathbf{Da}\Gamma^2}{4}, \quad (49)$$

$$\lim_{\substack{\xi(z)\to 0,\\ r_p\to 0}} K_1 = \frac{1}{2} + \frac{\Gamma\mathbf{Da}}{12}, \quad (50)$$

$$\lim_{r_p\to 0} K_2 = 1 + \frac{\mathbf{Pe}^2}{192} \quad (51)$$

Eq. (51) is consistent with that reported in Aris [22]. Eqn. (45) is a *linear homogeneous partial differential equation*, however, the coefficients K_0 and K_1 are both functions of z due to the arterial stenosis. To avoid this complication and noting that a *mild stenosis*, is present, one can neglect therefore the terms involving $\xi(z)$ from the transport coefficient and denote them by K_0^{approx} and K_1^{approx}. To extract the solution of Eq. (45), the following transformations are implemented:

$$C_{(0)}(z,t) = \Psi(x,t)\exp(-2K_0^{\text{approx}} t/\mathbf{Pe}) \quad (51)$$

$$t^* = \frac{t'}{R_0'^2 / D} \tag{52}$$

$$\eta = \frac{z'}{R_0'} - K_1^{\text{approx}} \mathbf{Pe} t^* \tag{53}$$

Furthermore, invoking the conditions (A6), (A7), the solution is derived as:

$$C_{(0)}(\eta, t^*) = \frac{1}{\sqrt{4\pi K_2 t^*}} \exp\left(-\frac{\eta^2}{4K_2 t^*} - 2K_0^{\text{approx}} \mathbf{Da} t^* \right) \tag{54}$$

It follows that:

$$C(\eta, r, t^*) = \left[1 + \frac{\mathbf{Da}\Gamma}{4}(1 - 2r^2) \right] C_{(0)} + \mathbf{Pe}(\mathbf{A} + X) \frac{\partial C_{(0)}}{\partial \eta} + \mathrm{O}(\mathbf{Da}^2) \tag{56}$$

The mean concentration C_m can be determined by taking the cross-sectional average of Eq.(56), i.e., $C_m(\eta, t^*) = 2\int_0^1 rC dr = C_{(0)}(\eta, t^*)$.

3. ASYMPTOTIC COMPUTATION VISUALIZATION

Extensive visualization of asymptotic results has been presented in **Figs. 2-8**. All biophysical data has been carefully checked and conforms with realistic physiological flow scenarios. Also axial velocity $u(r, z)$ and shear stress $\tau(r, z)$ can be plotted based on expressions (A5) and (A6) given in the **Appendix A**. The transport coefficients can also be evaluated for different stenotic scenarios and yield stress (rheological parameter) values.

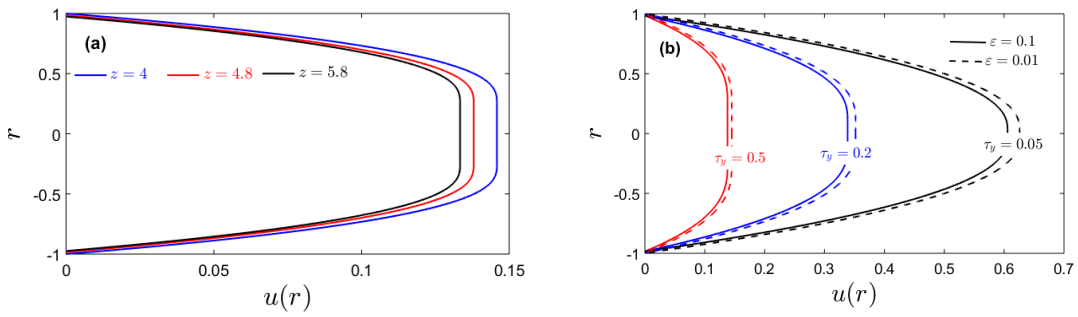

Fig. 2 Radial variation of blood velocity across the blood artery for fixed $l = 1, d = 4$ and $\delta = 0.4$; (a) different axial location but fixed yield stress $\tau_y = 0.5$ and aspect ratio ($\varepsilon = 0.1$) ,(b) different yield stress (τ_y) and aspect ratio (ε) but fixed axial location $(z = 4.8)$.

Figures 2a,b visualize the radial velocity $u(r)$ distributions across the arterial cross-section (a) at different axial location but fixed yield stress, $\tau_y = 0.5$ and aspect ratio ($\varepsilon = 0.1$) and (b) for different yield stress (τ_y) and aspect ratio (ε) but at fixed axial location $(z = 4.8)$. The other geometrical default parameters are $l = 1, d = 4$ and $\delta = 0.4$. **Figure 2a** clearly captures the plug flow velocity in the core region characterizing viscoplastic behavior (yield stress $\tau_y = 0.5$). With greater axial coordinate, z, the plug plateau is clearly reduced indicating that the core plug flow zone contracts with progress along the artery i.e. the effect of yield stress diminishes. **Figure 2b** shows that in the very weakly non-Newtonian case $(\tau_y = 0.05)$, essentially the classical parabolic distribution for radial velocity is computed. However, with greater yield stress $(\tau_y = 0.2, 0.5)$, the velocity profile morphs into the plug flow associated with stronger viscoplastic effect in the blood. These plots correspond to an intermediate axial coordinate value $(z = 4.8)$. The rheological nature of the radial blood flow distribution is clearly reproduced accurately in both figures and essentially higher yield stress effect induced a deceleration in the flow associated with greater viscous effects. This observation concurs with many other studies on yield stress hemodynamics, notably Sriyab [61] and also Venkatesan *et al*. [62], who both also considered the Casson model in mild stenotic flows.

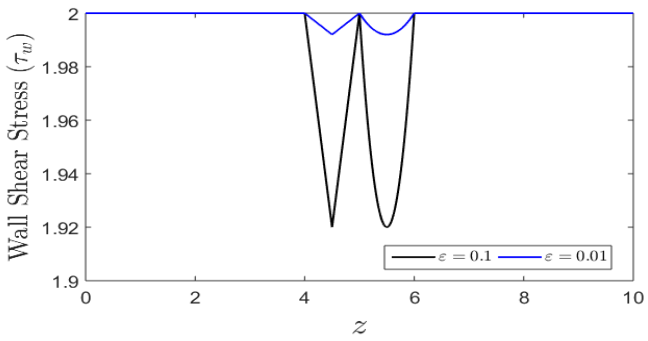

Fig. 3: Shear stress (τ) at the wall of blood artery at different axial location for different of aspect ratio (ε) with $l = 1, d = 4$ and $\delta = 0.4$.

Figure 3 depicts the wall shear stress (WSS), τ_w, evolution distributions with axial coordinate i.e. along the artery, for two different values of the aspect ratio (ε). Significantly higher wall shear stress is computed with greater aspect ratio owing to the greater resistance to hemodynamic transport, in particular at intermediate axial coordinate locations.

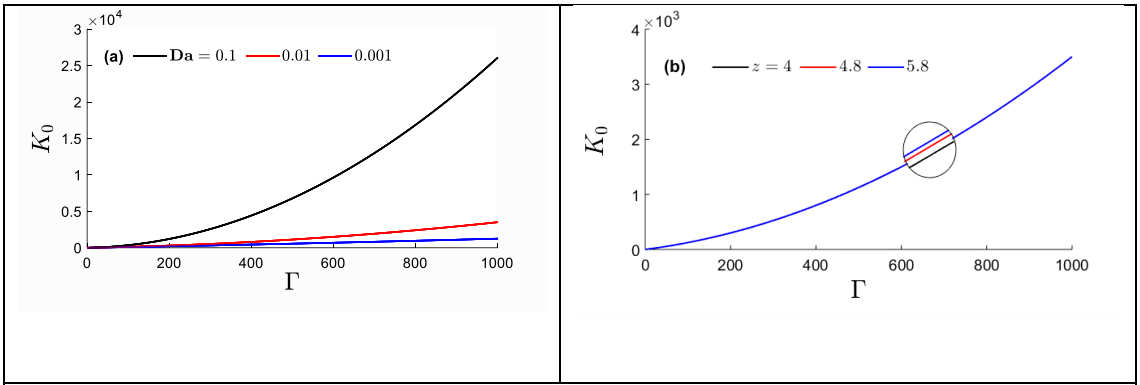

Fig. 4: Reaction coefficient Vs wall absorption for fixed $l=1, d=4$ and $\delta=0.4$; (a) different Damköhler numbers but fixed axial location ($z=5.5$), (b) different axial location but fixed Damköhler number (**Da** $=0.01$).

Figures 4(a,b) displays the reaction coefficient (K_0) versus wall absorption (Γ), for fixed $l=1, d=4$ and $\delta=0.4$; for (a) different Damköhler numbers but fixed axial location $(z=5.5)$ and (b) different axial location but fixed Damköhler numbers $(Da=0.01)$. Both K_0 and Γ, are related in Eq. (46) i.e. $K_0=\Gamma+\dfrac{\mathbf{Da}\Gamma^2}{4}+\varepsilon\xi(z)\Gamma$.

Damköhler number (**Da**) permits quantification of whether diffusion rates or reaction rates are more 'important' for defining a steady-state chemical distribution over the length and time scales of interest. It generally expresses the ratio of diffusion time to reaction time or alternatively the ratio of reaction rate to diffusion rate. Popular also in chemical engineering [63], **Da** is therefore intimately connected to characteristic diffusion and reaction times and this is why scaling is required in mathematical models. Two extremities are pertinent to comment on. The first, $\mathbf{Da}<<1$ implies that diffusion occurs much faster than the reaction and therefore diffusion attains an 'equilibrium' well prior to the reaction achieving equilibrium. The second, $\mathbf{Da}>>1$ indicates that the reaction

rate significantly exceeds the diffusion rate distribution and the regime is termed as being "diffusion-limited" (since diffusion is slowest, the diffusion characteristics dominate and the reaction is taken as assuming equilibrium instantaneously). For more realistic hemodynamic reactive flows, here **Da** values are varied between 0.001 and 0.1 [64]. **Fig 4a** shows that with increasing wall absorption (reaction) there is a monotonic growth in reaction coefficient (K_0). A significantly higher reaction coefficient is produced with increasing Damköhler number. The values considered for **Da** are all lower than unity as it is one of perturbation parameter in the present study. For $\mathbf{Da} = 0.001$ (i.e. $<<1$), the reaction coefficient remains largely invariant with a change in absorption parameter. However as **Da** is increased to 0.01 and thereafter to 0.1, a pronounced enhancement is induced in the reaction coefficient. Cleary for $\mathbf{Da} = 0.1$ the reaction rate is one-tenth of the diffusion rate and this is the strongest reaction rate scenario investigated. **Figure 4b** shows that with an increasing axial coordinate, at relatively low Damköhler number ($\mathbf{Da} = 0.01$ i.e. reaction rate is 100^{th} of the diffusion rate), a very weak increase in reaction coefficient (K_0) is generated with a large increase in the absorption parameter, Γ.

Figures. 5a-c show the evolution in convection coefficient (K_1) with the absorption parameter, Γ for (a) different Damköhler numbers with fixed yield stress ($\tau_y = 0.5$) and axial location ($z = 5.5$), (b) different yield stress (τ_y) with fixed Damköhler numbers $(\mathbf{Da} = 0.01)$ and axial location ($z = 5.5$) and (c) different axial location with fixed yield stress($\tau_y = 0.5$) and Damköhler numbers $(\mathbf{Da} = 0.01)$. Distinct from the reaction coefficient variation, here the convection coefficient is found to exhibit a linear growth relationship with the absorption parameter, Γ. Increasing Damköhler number (**Fig. 5a**) clearly stimulates a very steep ascent in convection coefficient, which is absent at much lower Damköhler numbers $(\mathbf{Da} = 0.001)$ is essentially invariant and $\mathbf{Da} = 0.01$ produces

only a very gentle growth in convection coefficient with Damköhler number. At zero absorption $(\Gamma = 0)$, the cases $\mathbf{Da} = 0.001$ and $\mathbf{Da} = 0.01$ have almost identical non-zero magnitudes of convection coefficient (K_1), although the values diverge substantially with increasing absorption parameter.

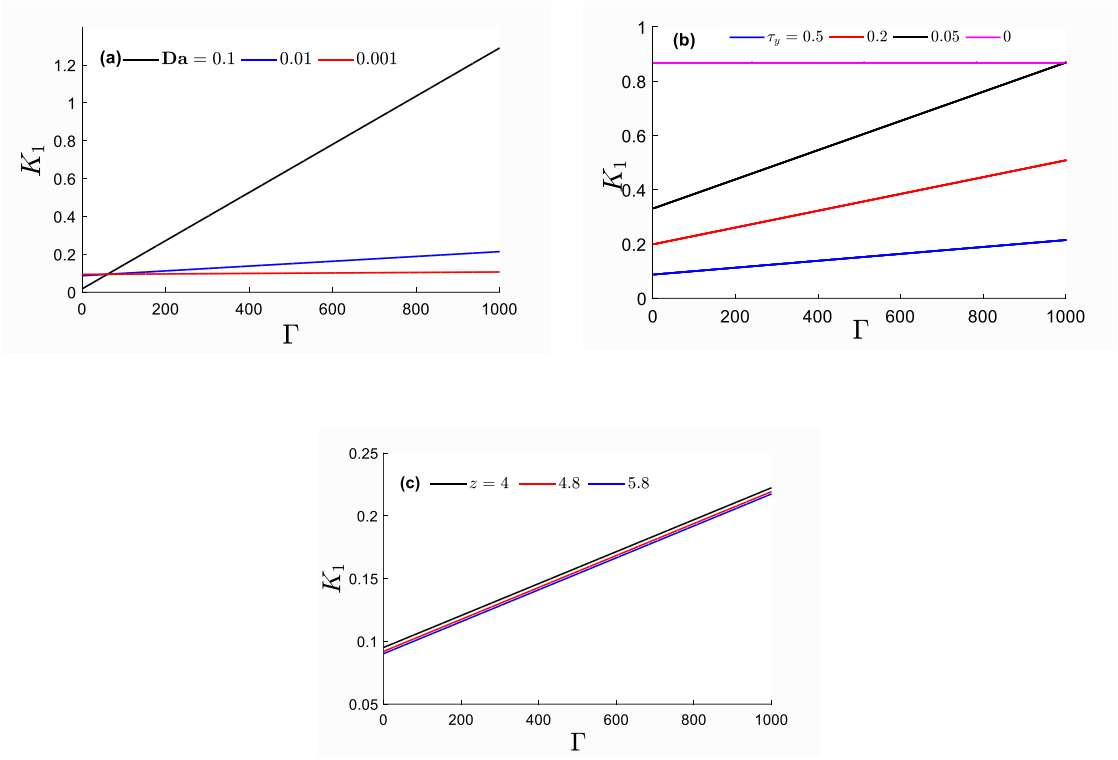

Fig. 5: Convection coefficient Vs wall absorption for fixed $l = 1, d = 4$ and $\delta = 0.4$; (a) different Damköhler numbers but fixed yield stress($\tau_y = 0.5$) and axial location ($z = 5.5$), (b) different yield stress (τ_y) but fixed Damköhler number ($\mathbf{Da} = 0.01$) and axial location ($z = 5.5$), (c) different axial location but fixed yield stress($\tau_y = 0.5$) and Damköhler number ($\mathbf{Da} = 0.01$).

Figure 5b shows that with progressively increasing yield stress i.e. stronger viscoplastic behavior of blood, there is a marked depletion in the convection coefficient value at all values of absorption (wall reaction) parameter. Weakly viscoplastic fluid $(\tau_y = 0.05)$ achieves maximum values of convection coefficient and strongly viscoplastic fluid $(\tau_y = 0.5)$ corresponds to minimal values. At zero absorption rate, however, for the different yield stress cases, the convection coefficient has distinct non-zero values. **Fig**.

5c indicates that there is a relatively weak decrease in convection coefficient with increasing axial coordinate value, irrespective of the absorption (wall reaction) parameter. **Figures 6** illustrates the evolution in relative dispersion coefficient $(K_2 / K_2^{\text{Newtonian}})$ with plug radius (r_p) for a variety of Péclet numbers $(\mathbf{Pe})$. In rheological flows, P\'eclet number quantifies the ratio of flow effects to diffusion effects and can describe whether particles are driven by flow $(\mathbf{Pe} > 1)$ or by their own diffusion $(\mathbf{Pe} < 1)$. **Pe** also relates convective and diffusive transport phenomena i.e. measures convective (or advective) transport rate to diffusive transport rate.

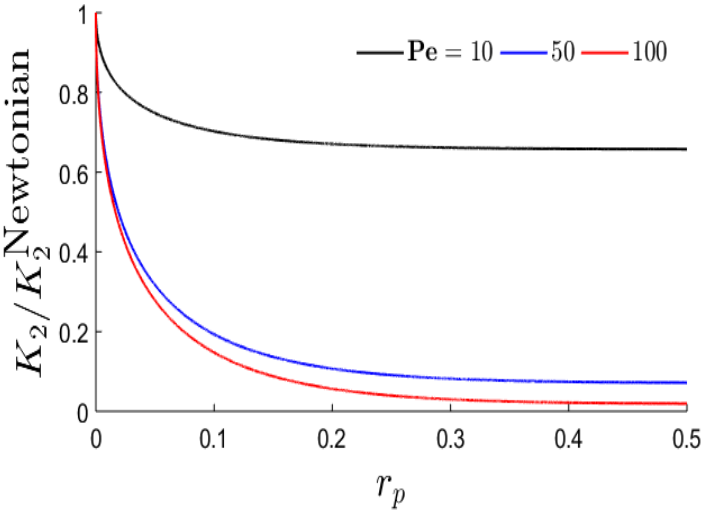

Fig. 6: Relative dispersion coefficient Vs plug radius for variety of Péclet numbers.

At all values of **Pe**, there is a strong decay in relative dispersion coefficient $(K_2 / K_2^{\text{Newtonian}})$ with plug radius (r_p) implying that as the plug zone widens the relative dispersion is suppressed. Although sharp descents are computed in all cases at low plug radius, the curves tend to plateau as plug radius increases exhibiting a tendency to invariance at a very high plug radius. At higher, Péclet number ($\mathbf{Pe} = 100$, for which the convective transport rate is 100 times the diffusion rate), relative dispersion coefficient $(K_2 / K_2^{\text{Newtonian}})$ is clearly minimized. The contrary is observed at the lowest P\'eclet

number ($\mathbf{Pe} = 10$, for which convective transport rate is 10 times the diffusion rate) and the magnitudes here are significantly higher at all values of plug radius. The results concur with findings in other studies including Huang and Tarbell [65].

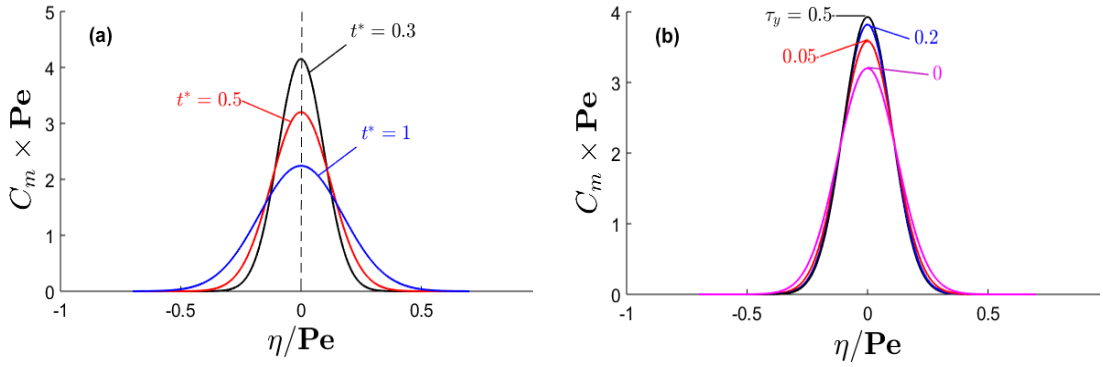

Fig. 7: Mean concentration distribution (a) at different times for fixed wall reaction rate ($\Gamma = 1$), yield stress ($\tau_y = 0.5$), Damköhler number ($\mathbf{Da} = 0.01$); and Péclet number ($\mathbf{Pe} = 10$) (b) variety yield stress at times $t^* = 0.5$ for fixed wall reaction rate ($\Gamma = 1$),Damköhler number ($\mathbf{Da} = 0.01$), and Péclet number ($\mathbf{Pe} = 10$).

Figures 7a-b depict the mean concentration distribution i.e. $C_m \times \mathbf{Pe}$ (a) at different times for fixed wall reaction rate $(\Gamma = 1)$, yield stress $(\tau_y = 0.5)$, Damköhler number $(\mathbf{Da} = 0.01)$ and Péclet number $(\mathbf{Pe} = 10)$ and (b) various yield stress at times $t^* = 0.5$ for fixed wall reaction rate $(\Gamma = 1)$, Damköhler number $(\mathbf{Da} = 0.01)$ and Péclet number $(\mathbf{Pe} = 10)$. The classical bell-shaped Taylor distribution is clearly captured in both figures. With progression in time (t^*), the peak magnitudes in mean concentration distribution i.e. $Cm \times \mathbf{Pe}$ are notably suppressed (**Fig. 7a**) for low values of $\eta / \mathbf{Pe}$ ($-0.2 < \eta / \mathbf{Pe} < +0.2$ approximately), but nevertheless remain symmetric about vertical axis at the origin. However, at larger $\eta / \mathbf{Pe}$ values this trend is reversed and a marked elevation in mean concentration distribution i.e. $C_m \times \mathbf{Pe}$ is observed. In all profiles converge in an asymptotically smooth fashion to vanishing values of $C_m \times \mathbf{Pe}$ at higher $\eta / \mathbf{Pe}$ values. **Figure 7b** shows that Newtonian fluids $(\tau_y = 0)$ achieve the lowest values of mean concentration distribution i.e. $C_m \times \mathbf{Pe}$, and with greater yield stress

($\tau_y = 0.05, 0.2, 0.5$) progressively higher values are computed. However, this pattern is confined to smaller values of $\eta / \mathbf{Pe}$ values ($-0.1 < \eta / \mathbf{Pe} < +0.1$ approximately). At larger values of $\eta / \mathbf{Pe}$ Newtonian fluid is found to generate slightly higher magnitudes of mean concentration distribution i.e. $C_m \times \mathbf{Pe}$, whereas increasingly viscoplastic behavior of the Casson blood i.e. greater yield stress ($\tau_y = 0.05, 0.2, 0.5$) manifests in a lower mean concentration distribution i.e. $C_m \times \mathbf{Pe}$.

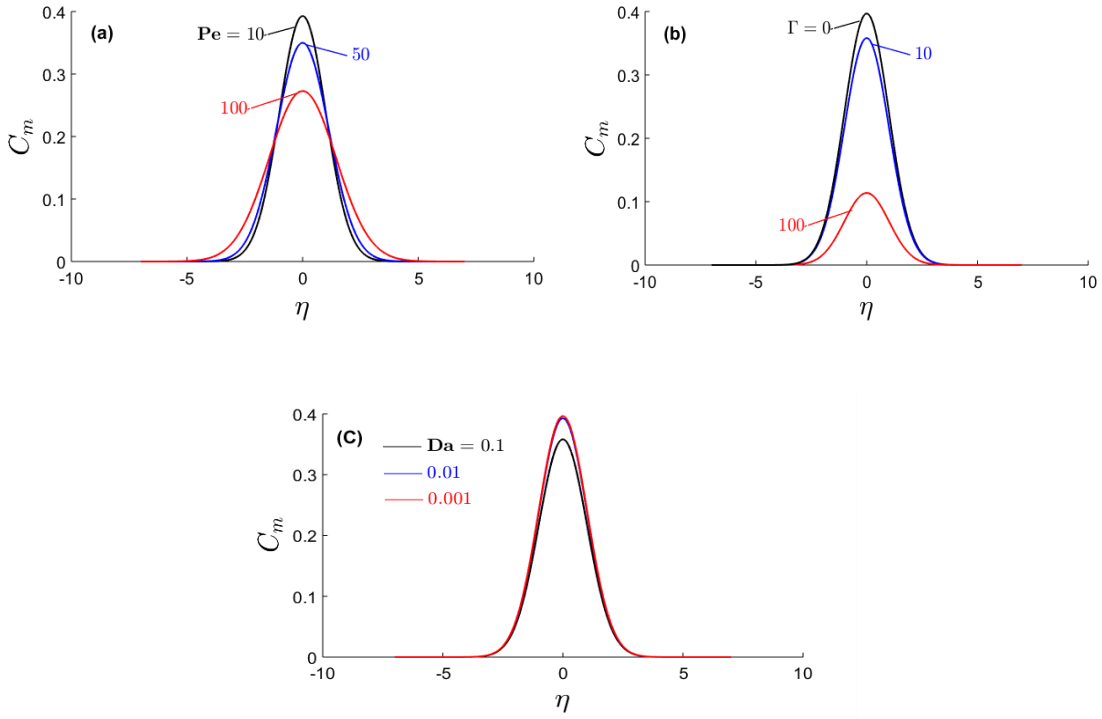

Fig. 8: Mean concentration at time $t^* = 0.5$ for (a) variety of Péclet numbers but fixed wall reaction rate ($\Gamma = 1$), yield stress ($\tau_y = 0.5$) and Damköhler number ($\mathbf{Da} = 0.01$); (b) variety of wall Reaction for fixed Damköhler number ($\mathbf{Da} = 0.01$), yield stress ($\tau_y = 0.5$) and Péclet number ($\mathbf{Pe} = 10$); (c) variety of Damköhler number but fixed wall reaction rate ($\Gamma = 1$), yield stress ($\tau_y = 0.5$) and Péclet number ($\mathbf{Pe} = 10$).

Finally, **Figs 8a-c** illustrate the mean concentration profiles versus at time $t^* = 0.5$ for (a) various Péclet numbers under prescribed wall reaction rate ($\Gamma = 1$), yield stress ($\tau_y = 0.5$) and Damköhler number ($\mathbf{Da} = 0.01$); (b) various wall reaction (absorption) parameters for fixed Damköhler number ($Da = 0.01$), yield stress ($\tau_y = 0.5$) and Péclet number ($\mathbf{Pe} = 10$); (c) various Damköhler numbers with fixed wall reaction rate ($\Gamma = 1$), yield

stress ($\tau_y = 0.5$) and Péclet numbers ($\mathbf{Pe} = 10$). Significant suppression in Cm magnitudes is induced with increasing Péclet numbers at low values of η; however, the opposite effect is caused at larger values of η (**Fig. 8a**). The maximum mean concentration (C_m) is computed in **Fig. 8b** for zero wall reaction rate (Γ) and a strong depletion is observed in C_m; this trend is sustained at all values of η. **Fig. 8c** reveals that a very large enhancement in Damköhler number (a hundred fold from $\mathbf{Da} = 0.001$ to 0.1) produces a slight depression in mean concentration (C_m) at very small values of η; however at higher values the discrepancy there is a trivial difference.

4.CONCLUSIONS

A theoretical study of the transport of species in streaming blood flow through a rigid artery in the presence of multi-irregular stenosis has been conducted. The carrier fluid i.e., blood is assumed to be non-Newtonian fluid (Casson's viscoplastic model is used) and the arterial wall is considered to be rigid. A robust model is developed for non-Newtonian flow and hydrodynamic dispersion with the first-order chemical reaction on the arterial boundary in multiple irregular stenosed arterial geometries. Multiple scale solutions of the non-dimensional boundary value problem. asymptotic expressions are developed for velocity and shear stress. Extensive visualization of velocity, concentration, and other flow characteristics is included for various stenotic scenarios, Péclet number, and Damköhler number. The asymptotic solutions have shown that:

(I) At all values of Péclet number ($\mathbf{Pe}$), there is a marked decrease in relative dispersion coefficient ($K_2 / K_2^{\text{Newtonian}}$) with plug radius ($r_p$).

(II) With progression in time (t^*), the peak magnitudes in mean concentration distribution i.e. $C_m \times \mathbf{Pe}$, are strongly reduced for low values of $\eta / \mathbf{Pe}$ whereas the opposite behavior is computed at larger $\eta / \mathbf{Pe}$ values..

(III) Newtonian fluids $(\tau_y = 0)$ achieve the lowest values of scaled mean concentration distribution i.e. $C_m \times \mathbf{Pe}$, and with greater yield stress $(\tau_y = 0.05, 0.2, 0.5)$ progressively higher values in mean concentration are found, although this is restricted to smaller values of $\eta / \mathbf{Pe}$; at larger values of $\eta / \mathbf{Pe}$, Newtonian fluid achieves weakly greater mean concentration whereas increasingly viscoplastic behavior of the Casson blood i.e. greater yield stress produces a drop in mean concentration distribution i.e. $C_m \times \mathbf{Pe}$.

(IV) There is a substantial reduction in mean concentration C_m magnitudes with increasing Péclet number at low values of η; however, the converse response is produced at larger values of η. (**Fig. 8a**).

(V) A comparatively small reduction in convection coefficient is induced with increasing axial coordinate value, irrespective of the absorption (wall reaction) parameter.

(VI) Increasing yield stress i.e. viscoplasticity of the blood results in a noticeable suppression in the convection coefficient value at all values of absorption (wall reaction) parameter.

(VII) Increasing wall absorption (reaction) produces a monotonic growth in zeroth-order reaction coefficient distribution (K_0) whereas a significantly greater reaction coefficient is associated with increasing Damköhler number.

(VIII) Significantly higher wall shear stress is produced with a larger aspect ratio of the stenotic regime.

(IX) In the very weakly non-Newtonian case $(\tau_y = 0.05)$, the classical parabolic distribution for radial velocity is retrieved; however, with greater yield stress $(\tau_y = 0.2, 0.5)$, the velocity profile topology is modified into the plug flow associated with stronger viscoplastic effects in the blood.

The current study has revealed some interesting phenomena in pulsatile biorheological flow with mass transfer and reactive dispersion. Multi-scale asymptotics has proved to be a very robust tool in analyzing such flows of relevance to hemodynamics e.g. plaque deposition in the intima layer of arteries (atherogenesis). Future studies may consider alternative rheological models e.g. micropolar [31, 41] and efforts in this direction are currently under consideration.

ACKNOWLEDGEMENTS:

The authors would like to thanks to thank Prof. Igor Pažanin, University of Zagreb, for his helpful suggestions. Furthermore both authors also appreciate the helpful comments of the reviewers which have improved the manuscript in clarity.

CONFLICT OF INTEREST

The authors declare that they have no conflict of interest.

APPENDIX

After using scaling defined in the present study, the non-dimensional form of the momentum Eq. (8) is:

$$\frac{1}{r}\frac{\partial}{\partial r}(r\tau) = 4 \text{ in } \Omega, \tag{A1}$$

The *non-dimensional* form of the constitutive Eq. (9) becomes

$$-\frac{\partial u}{\partial r} = \begin{cases} \left(\sqrt{\tau} - \sqrt{\tau_y}\right)^2 & \text{if} \quad \tau \geq \tau_y \\ 0 & \text{if} \quad \tau \leq \tau_y \end{cases} \tag{A2}$$

The non-dimensional boundary conditions (10) emerge as :

$$u(r,z) = 0, \quad \text{on} \quad \partial\Omega, \tag{A3}$$

$$\tau < \infty, \quad \text{at} \quad r = 0. \tag{A4}$$

Here the reference velocity (u_R) is taken as $u_R = -(R_0^2 / 4\mu')\partial p' / \partial z'$. Solving Eqs. (A1) and (A2) using boundary conditions (A3) and (A4) we get:

$$\tau(r,z) = \begin{cases} 2r, & \text{if} \ \ \tau_0 \geq \tau_y, \\ \tau_y, & \text{if} \ \ \tau_0 \leq \tau_y. \end{cases} \tag{A5}$$

$$u(r,z) = \begin{cases} (R^2 - r^2) + 2r_p(R-r) - \dfrac{8\sqrt{r_p}}{3}(R^{3/2} - r^{3/2}), & \text{if} \quad r \geq r_p, \\ R^2 + 2r_p R - \dfrac{8}{3}\sqrt{r_p}R^{3/2} - \dfrac{1}{3}r_p^2, & \text{if} \quad r \leq r_p. \end{cases} \tag{A6}$$

Here, $r_p = \tau_y / 2$ is the plug radius up to which no velocity shear effect is observed.

The radius of the blood artery is $R = 1 - \varepsilon\xi(z)$, by using this in Eq. (A6) and collecting like powers of ε we get:

$$u(r,z) = u_0(r,z) + \varepsilon u_1(r,z) + \mathrm{O}(\varepsilon^2), \tag{A7}$$

where

$$u_0(r,z) = \begin{cases} (1 - r^2) + 2r_p(1-r) - \dfrac{8\sqrt{r_p}}{3}(1 - r^{3/2}), & \text{if} \quad r \geq r_p, \\ 1 + 2r_p - \dfrac{8}{3}\sqrt{r_p} - \dfrac{1}{3}r_p^2, & \text{if} \quad r \leq r_p. \end{cases} \tag{A8}$$

REFERENCES:

1. Mandelbaum I, Burns WH (1965) Pulsatile and nonpulsatile blood flow. JAMA 191(8):657–660.

2. Zamir M (2000) The physics of pulsatile flow. Springer-Verlag, New York.

3. Silver DM, Farrell RA, Langham ME, O'Brien V, Schilder P (1989) Estimation of pulsatile ocular blood flow from intraocular pressure. Acta Ophthalmol (Copenh) 67(S191):25–29.

4. Fukushima T, Homma T, Harakawa K, Sakata N, Azuma T (1988) Vortex generation in pulsatile flow through arterial bifurcation models including the human carotid artery. J Biomech Eng 110(3):166–171.

5. Moore JE, Ku DN, Zarins CK, Glagov S (1992) Pulsatile flow visualization in the abdominal aorta under differing physiologic conditions: implications for increased susceptibility to atherosclerosis. J Biomech Eng 114:391–397.

6. Daripa P, Dash RK (2002) A numerical study of pulsatile blood flow in an eccentric catheterized artery using a fast algorithm. J Eng Math 42(1):1–22.

7. Boyd J, Buick JM (2008) Three-dimensional modelling of the human carotid artery using the lattice Boltzmann method: II. Shear analysis. Phys Med Biol 53(20):5781–5795.

8. Zaman A, Ali N, Bég OA (2016) Numerical study of unsteady blood flow through a vessel using Sisko model. Eng Sci Technol Int J 19(1):538–547.

9. Ponalagusamy R (2015) Chapter 3 - Biological Study on Pulsatile Flow of Herschel-Bulkley Fluid in Tapered Blood Vessels. In: Tran QN, Arabnia H (eds) Emerging Trends in Computational Biology, Bioinformatics, and Systems Biology. Morgan Kaufmann, Boston, pp 39–50.

10. Chandran KB, Rittgers SE, Yoganathan AP (2012) Biofluid mechanics: The human circulation, Second Edition. CRC Press.

11. Casson N (1959) A flow equation for pigment-oil suspensions of the printing ink type. Rheol Disperse Syst.

12. Blair GWS (1959) An equation for the flow of blood, plasma and serum through glass capillaries. Nature 183(4661):613–614.

13. Copley AL (1960) Apparent viscosity and wall adherence of blood systems. In: Flow properties of blood and other biological systems. Pergamon Press, Oxford, UK.

14. Merrill EW, Benis AM, Gilliland ER, Sherwood TK, Salzman EW (1965) Pressure-flow relations of human blood in hollow fibers at low flow rates. J Appl Physiol 20(5):954–967.

15. Charm S, Kurland G (1965) Viscometry of human blood for shear rates of 0-100,000 sec^{-1}. Nature 206(4984):617–618.

16. Blair GWS, Spanner DC (1974) Introduction to biorheology. Elsevier Scientific Publ. Co. Aroesty J, Gross JF (1972) Pulsatile flow in small blood vessels—I. Biorheology 9(1):33–43.

17. Aroesty J, Gross JF (1972) Pulsatile flow in small blood vessels—I. Biorheology 9(1):33–43.

18. Chaturani P, Palanisamy V (1990) Casson fluid model for pulsatile flow of blood under periodic body acceleration. Biorheology 27(5):619–630.

19. Akbar NS, Tripathi D, Bég OA, Khan ZH (2016) MHD dissipative flow and heat transfer of Casson fluids due to metachronal wave propulsion of beating cilia with thermal and velocity slip effects under an oblique magnetic field. Acta Astronaut 128:1–12.

20. Rohlf K, Tenti G (2001) The role of the Womersley number in pulsatile blood flow: A theoretical study of the Casson model. J Biomech 34(1):141–148.

21. Taylor GI (1953) Dispersion of soluble matter in solvent flowing slowly through a tube. Proc R Soc Lond Ser Math Phys Sci 219(1137):186–203.

22. Aris R (1956) On the dispersion of a solute in a fluid flowing through a tube. Proc R Soc Lond Ser Math Phys Sci 235(1200):67–77.

23. McDonald DA (1960) Blood Flow in Arteries. E. Arnold. Barton NG (1983) On the method of moments for solute dispersion. J Fluid Mech 126:205–218.

24. Mazumder BS, Das SK (1992) Effect of boundary reaction on solute dispersion in pulsatile flow through a tube. J Fluid Mech 239:523–549.

25. Paul S, Mazumder BS (2009) Transport of reactive solutes in unsteady annular flow subject to wall reactions. Eur J Mech - B/Fluids 28(3):411–419.

26. Wu Z, Fu X, Wang G (2016) On spatial pattern of concentration distribution for Taylor dispersion process. Sci Rep 6(1):20556.

27. Wu Z, Fu X, Wang G (2016) On spatial pattern of concentration distribution for Taylor dispersion process. Sci Rep 6(1):20556.

28. Bhargava R, Rawat S, Takhar HS, Anwar Bég O (2007) Pulsatile magneto-biofluid flow and mass transfer in a non-Darcian porous medium channel. Meccanica 42(3):247–262.

29. Zueco J, Bég OA Network numerical simulation applied to pulsatile non-Newtonian flow through a channel with couple stress and wall mass flux effects. Int J Appl Math Mech 5(2):1–16.

30. Bég OA, Bég TA, Bhargava R, Rawat S, Tripathi D (2012) Finite element study of transient pulsatile magneto-hemodynamic non-newtonian flow and drug diffusion in a porous medium channel. J Mech Med Biol 12(4):1250081.

31. Ravi Kiran G, Radhakrishnamacharya G, Bég OA (2016) Peristaltic flow and hydrodynamic dispersion of a reactive micropolar fluid-simulation of chemical effects in the digestive process. J Mech Med Biol 17(1):1750013.

32. Sharp MK (1993) Shear-augmented dispersion in non-Newtonian fluids. Ann Biomed Eng 21(4):407–415.

33. Dash RK, Jayaraman G, Mehta KN (2000) Shear augmented dispersion of a solute in a casson fluid flowing in a conduit. Ann Biomed Eng 28(4):373–385.

34. Sankarasubramanian R, Gill WN (1973) Unsteady convective diffusion with interphase mass transfer. Proc R Soc Lond Math Phys Sci 333(1592):115–132.

35. Nagarani P, Sarojamma G, Jayaraman G (2004) Effect of boundary absorption in dispersion in casson fluid Flow in a tube. Ann Biomed Eng 32(5):706–719.

36. Rana J, Murthy PVSN (2016) Solute dispersion in pulsatile Casson fluid flow in a tube with wall absorption. J Fluid Mech 793:877–914.

37. Roy AK, Saha AK, Debnath S (2019) Hydrodynamic dispersion of solute under homogeneous and heterogeneous reactions. Int J Heat Technol 37(2):387–397.

38. Debnath S, Saha AK, Mazumder BS, Roy AK (2017) Dispersion phenomena of reactive solute in a pulsatile flow of three-layer liquids. Phys Fluids 29(9):097107.

39. Debnath S, Saha AK, Mazumder BS, Roy AK (2019) Transport of a reactive solute in a pulsatile non-Newtonian liquid flowing through an annular pipe. J Eng Math 116(1):1–22.

40. Ganz P, Harrington DP, Gaspar J, Barry WH (1983) Phasic pressure gradients across coronary and renal artery stenoses in humans. Am Heart J 106(6):1399–1406.

41. Zaman A, Ali N, Bég OA (2016) Numerical simulation of unsteady micropolar hemodynamics in a tapered catheterized artery with a combination of stenosis and aneurysm. Med Biol Eng Comput 54(9):1423–1436.

42. Zaman A, Ali N, Beg OA, Sajid M (2016) Unsteady two-layered blood flow through a w-shaped stenosed artery using the generalized Oldroyd-B fluid model. ANZIAM J 58:96–118.

43. Ali N, Zaman A, Sajid M, Bég, OA, Shamshuddin, M, Kadir, A (2018) Numerical simulation of time-dependent nonnewtonian nanopharmacodynamic transport phenomena in a tapered overlapping stenosed arter. Nanosci Technol Int J 9(3).

44. Dubey A, Vasu B, Bég OA, Gorla, RSR, Kadir, A (2020) Computational fluid dynamic simulation of two-fluid non-Newtonian nanohemodynamics through a diseased artery with a stenosis and aneurysm. Comput Methods Biomech Biomed Engin 23(8):345–371.

45. Srivastava VP, Saxena M (1994) Two-layered model of Casson fluid flow through stenotic blood vessels: Applications to the cardiovascular system. J Biomech 27(7):921–928.

46. Priyadharshini S, Ponalagusamy R (2019) Mathematical modelling for pulsatile flow of Casson fluid along with magnetic nanoparticles in a stenosed artery under external magnetic field and body acceleration. Neural Comput Appl 31(3):813–826.

47. Mustapha N, Mandal PK, Johnston PR, Amin N (2010) A numerical simulation of unsteady blood flow through multi-irregular arterial stenoses. Appl Math Model 34(6):1559–1573.

48. Johnston PR, Kilpatrick D (1991) Mathematical modelling of flow through an irregular arterial stenosis. J Biomech 24(11):1069–1077.

49. Andersson HI, Halden R, Glomsaker T (2000) Effects of surface irregularities on flow resistance in differently shaped arterial stenoses. J Biomech 33(10):1257–1262.

50. Chakravarty S, Mandal PK, Sarifuddin (2005) Effect of surface irregularities on unsteady pulsatile flow in a compliant artery. Int J Non-Linear Mech 40(10):1268–1281.

51. Mustapha N, Chakravarty S, Mandal PK, Amin N (2008) Unsteady response of blood flow through a couple of irregular arterial constrictions to body acceleration. J Mech Med Biol 8(3):395–420.

52. Fowler NO, Cubberly R, Dorney E (1954) Pulmonary blood distribution and oxygen diffusion in mitral stenosis. Am Heart J 48(1):1–7.

53. Valencia A, Villanueva M (2006) Unsteady flow and mass transfer in models of stenotic arteries considering fluid-structure interaction. Int Commun Heat Mass Transf 33(8):966–975.

54. Zaman A, Ali N, Anwar Bég O, Sajid M (2016) Heat and mass transfer to blood flowing through a tapered overlapping stenosed artery. Int J Heat Mass Transf 95:1084–1095.

55. Olgac U, Kurtcuoglu V, Poulikakos D (2008) Modeling of blood-wall low-density lipoprotein mass transport in dependence of shear stress 41:S277.

56. Kaazempur-Mofrad MR, Wada S, Myers JG, Ethier CR (2005) Mass transport and fluid flow in stenotic arteries: Axisymmetric and asymmetric models. Int J Heat Mass Transf 48(21):4510–4517.

57. Yang N, Vafai K (2008) Low-density lipoprotein (LDL) transport in an artery – A simplified analytical solution. Int J Heat Mass Transf 51(3):497–505.

58. Moore JA, Ethier CR (1997) Oxygen mass transfer calculations in large arteries. J Biomech Eng 119(4):469–475.

59. Gessner Fred B. (1973) Brief reviews: Hemodynamic theories of atherogenesis. Circ Res 33(3):259–266

60. Ethier CR (2002) Computational modeling of mass transfer and links to atherosclerosis. Ann Biomed Eng 30(4):461–471.

61. Sriyab S (2014) Mathematical analysis of non-Newtonian blood flow in stenosis narrow arteries. Comput Math Methods Med 2014:1–10.

62. Venkatesan J, Sankar DS, Hemalatha K, Yatim Y (2013) Mathematical analysis of Casson fluid model for blood rheology in stenosed narrow arteries. J Appl Math 2013:1–11.

63. Bart H-J (2001) Reactive mass transfer. In: Bart H-J (ed) Reactive extraction. Springer, Berlin, Heidelberg, pp 51–130.

64. Baskurt OK, Hardeman MR, Rampling MW, Meiselman HJ (2007) Handbook of hemorheology and hemodynamics. IOS Press.

65. Huang ZJ, Tarbell JM (1997) Numerical simulation of mass transfer in porous media of blood vessel walls. Am J Physiol 273(1):H464–477.